Brightness and virtual source size of a supersonic deuterium beam

Thomas Reisinger,[1,*] Martin M. Greve,[1] Sabrina D. Eder,[1] Gianangelo Bracco,[1,2] and Bodil Holst[1]
[1]*Department of Physics and Technology, University of Bergen, Allégaten 55, 5007 Bergen, Norway*
[2]*Department of Physics and CNR-IMEM, University of Genova, V. Dodecaneso 33, 16146 Genova, Italy*
(Received 11 November 2011; published 3 October 2012)

Supersonic beams have numerous applications in research fields ranging from spectroscopy with nanodroplets to surface science and matter-wave microscopy. Thus, measurement and prediction of their properties is of considerable interest. In this paper we present measurements of the virtual-source size and its brightness, as well as the terminal speed and terminal speed ratio of a supersonic deuterium (D_2) beam. The speed distribution data were measured with time-of-flight experiments and Fresnel zone-plate imaging was used to measure virtual source size. The point-spread function of the zone plate was simulated based on the measured wavelength distribution and used to extract the width of the virtual source and its brightness from the focus measurement. The experiments were carried out with a 10-μm-diameter nozzle and a source temperature of $T_0 = 310$ K in the pressure range $p_0 = 3$–171 bars and for $T_0 = 106$ K in the pressure range $p_0 = 3$–131 bars. We found that using deuterium as opposed to helium results in a virtual source that is about a factor 2 brighter under similar stagnation conditions. A comparison between the measured data and the predictions from a theoretical model based on the Boltzmann equation, which explicitly include the coupling between translational and rotational degrees of freedom as well as the real-gas properties of D_2, resulted in good correspondence for the two different interaction potentials we tried. A careful comparison with the experimental results shows that the potential by Buck *et al.* [J. Chem. Phys. **78**, 4439 (1983)] is moderately better than the Lennard-Jones potential at describing the expansion dynamics.

DOI: 10.1103/PhysRevA.86.043804 PACS number(s): 37.20.+j, 03.75.−b, 47.40.Ki, 42.79.Ci

I. INTRODUCTION

When gas at high pressure expands supersonically into a vacuum chamber via a small nozzle it forms a neutral beam of high intensity and narrow energy distribution [1]. These properties make supersonic molecular beams useful in many different research fields such as surface science [2], laser spectroscopy, and magnetic and electric resonance spectroscopy [3–5]. For example, scattering of supersonic helium beams has been used to study the cleavage planes of organic single crystals [6], the relaxation of well-ordered surface ripples [7], and the dynamics of melting surfaces [8] and has been a very important tool for the investigation of oxide surfaces [9–11].

Helium beams have been used also in focusing applications, where the focusing element is a free-standing Fresnel zone plate [12] or mirror [13–15], and recently the first microscopic images using neutral helium atoms have been recorded [16,17]. Supersonic deuterium (D_2) beams are used to inject fuel into toroidal plasma fusion experiments [18] and as jet target in high-energy physics experiments [19,20]. Recently they have been also employed in matter-wave experiments [21] where deuterium was used as an alternative to helium. This is because it has the same atomic mass, 4, at which mass the chambers background gas contributes a relatively small signal background. In addition, the polarizability of D_2 is about a factor of three larger than that of helium [22], which means that it can be detected more efficiently in electron-bombardment detectors. Moreover, supersonic helium beams are characterized by a particularly narrow speed distribution due to the large scattering cross section of helium at low temperatures. This, however, comes at the cost of an increase in virtual source size and loss of source brightness [23–25]. Here we show that the supersonic expansion of D_2, on the other hand, results in a comparatively brighter source with a broader speed distribution. An increase in source brightness and detection efficiency of the beam is of benefit in a large array of diffraction and dynamic scattering experiments, including experiments with coherent beams at high spatial resolution [26].

In this article we study the expansion of molecular deuterium (D_2) from a 10-μm-diameter nozzle at two nozzle temperatures ($T_0 = 310$ K and 106 K) and over a wide pressure range: $p_0 = 3$–171 bars (warm nozzle) and 3–131 bars (cold nozzle). For these experimental conditions we performed time-of-flight (TOF) experiments to measure the terminal speed and the terminal speed ratio of the beam. The latter is defined as the ratio between the terminal speed and the width of the velocity distribution. Moreover, we have investigated the focusing of the deuterium beam by means of free-standing Fresnel zone plates and studied the image of the virtual source for the different stagnation conditions. For an accurate measurement of the virtual source size and its brightness we corrected the image by accounting for the zone plate's point-spread function (PSF). We calculated the latter by solving the Fresnel diffraction integral and averaging over the measured terminal speed (de Broglie wavelength) distribution. This method of analysis of focusing data was not yet used in our previous work [25], but is also more important here due to the larger wavelength-spread of the D_2 source when compared to helium.

In addition to experimental results we present a theoretical model that we use to predict terminal speed, speed ratio, and virtual source size. The model takes into account the

*Present address: Karlsruhe Institute of Technology, Institute of Nanotechnology, Hermann-von-Helmholtz-Platz 1, 76344 Eggenstein-Leopoldshafen, Germany; treisinger@gmail.com

quantum-mechanical scattering cross section of D_2, which we calculated for two different interaction potentials, namely, the empirical Lennard-Jones potential [27] and the potential determined by Buck *et al*. [28] to explain the results of crossed molecular beam experiments. The comparison between theory and experiment showed that the latter potential is better at predicting the expansion's properties of D_2. Overall the experimental verification described in the following sections shows that the developed theoretical model can be used as a predictive tool to plan future experiments that require a coherent D_2 beam.

II. EXPERIMENTAL METHOD

The apparatus used in the present study was designed for helium-scattering experiments [10] and helium microscopy [16]. Further details of the setup can be found elsewhere [29,30]. The ultra-high-vacuum system is shown schematically in Fig. 1. It consists of eight differentially pumped chambers. For all experiments a nozzle with diameter $d_n = (10 \pm 1)\ \mu$m was used. The deuterium pressure applied to the nozzle was varied in the range 1–180 bars above atmosphere, which was measured with a Bourdon gauge, resulting in an uncertainty of $\pm 1\%$ above $p_0 = 100$ bars and ± 1 bar below for the pressure readings. A liquid-nitrogen cryostat and a heating wire are used to manipulate the nozzle temperature in the range 100 K–400 K. In the third pumping stage, the beam is modulated by a movable chopper disk for the TOF measurements. The disk was removed from the beam axis during focusing experiments. The fifth chamber houses the zone plate that can be precisely aligned with the beam axis or moved clear of the beam using a motorized stage. In the wall separating the sixth and seventh pumping stages an x-y piezo table with a maximum range of 80 μm is integrated. On the piezo table we mounted a 25-μm-by-5-mm slit aperture for the TOF measurement or a 10-μm-diameter hole aperture for the focus width measurement. The aperture together with the piezo table can be moved in and out of the beam using a manual x-y stage. Finally, the beam is detected by a custom-built electron-bombardment detector with magnetic mass selection located in chamber 8 [31] and with an efficiency of about about 5×10^{-6} for D_2. The signal from the channeltron is preamplified, then transmitted to a CAMAC system via a fiber-optic link. A counter module or a TOF module processes the signal, which is then recorded using a Labview-based computer system.

One of the recorded TOF data sets is shown in Fig. 2. It was fitted with a Gaussian function to extract the most probable TOF and the full width at half maximum (FWHM) of the TOF distribution. The flight-time, FWHM, and chopper-to-detector distance are corrected based on calibration experiments. The detector was deliberately put at two different positions along the beam axis for the two different nozzle temperatures. The result of the chopper-to-detector distance calibration measurement (see [30]) was $L_{CD} = 2028.4 \pm 1.0$ mm for the warm-nozzle beam experiments and $L_{CD} = 2001.4 \pm 1.0$ mm in the case of the cold nozzle beam. The corrected TOF distribution is shown in Fig. 2 with a dashed (blue) line. For this study we have measured terminal speed and terminal speed-ratio of the deuterium beam in the source-pressure range $p_0 = 3$–171 bars for a nozzle temperature of $T_0 = 310$ K. For the cold nozzle temperature of $T_0 = 106$ K the higher flow through the nozzle causes the background pressure in the source chamber to reach critical levels already at lower nozzle pressures. This limited our experiments to a maximum pressure of 131 bars.

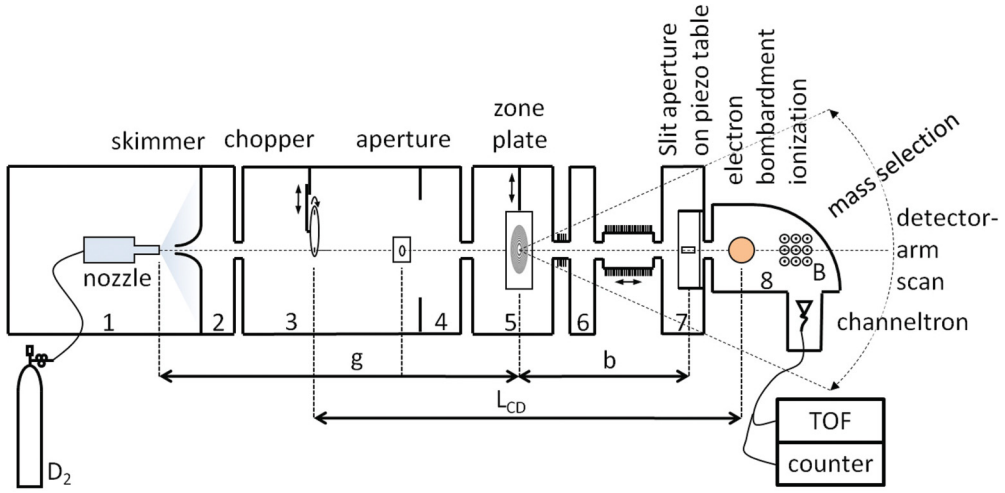

FIG. 1. (Color online) Schematic of experimental setup. Pressurized deuterium (D_2) gas expands into a high-vacuum chamber via a 10-μm-diameter nozzle. A skimmer and a circular aperture (both 400 μm diameter) collimate the beam onto a free-standing Fresnel zone plate. The skimmer diameter is larger than the virtual source, so that the zone plate creates an image of the virtual source in the plane of the hole aperture which is mounted on a piezo table. The position of the detector and piezo chambers along the beam axis (b) can be changed by expanding or contracting bellows within a range of about 160 mm, allowing the position to be optimized to the image plane of the zone plate. The width of the virtual source is determined by stepping the aperture across the image using the piezo table or the stepper motor driven detector arm whose center of rotation is in the plane of the zone plate. The beam is detected by an electron-bombardment detector with a magnetic sector for mass selection. The ions are counted using a channeltron. For TOF measurements a mechanical chopper is moved into the beam, the zone plate removed, and the detector signal recorded using TOF electronics, which receives a trigger signal from the chopper.

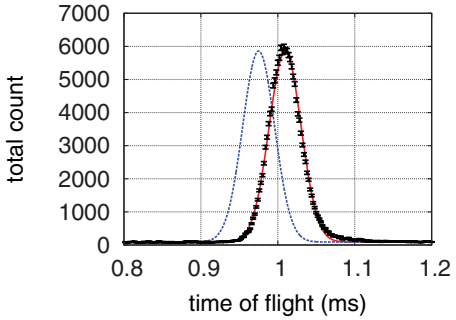

FIG. 2. (Color online) Time-of-flight spectrum for a supersonic deuterium beam at nozzle pressure $p_0 = 150$ bars and $T_0 = 310$ K is shown as black triangles. The error bars show statistical uncertainty. The continuous (red) line is the Gaussian curve fit of the data set. The calibrated and deconvolved distribution is shown as the dashed (blue) line, which corresponds to a terminal speed of 2080 ± 4 m/s and speed ratio 33.0 ± 0.2. These corresponding TOF distributions were used to simulate the chromatic PSF of the zone plates, which made it possible to deconvolve the images of the virtual source.

With the chopper removed from the beam line, we measured the virtual source width of the deuterium expansion by scanning across the image produced by a Fresnel zone plate with a 10-μm-diameter hole aperture. The scanning aperture was stepped across the focus using the piezo table. To examine the full diffraction image including the zeroth order of the zone plate the same was achieved by rotating the whole detector arm, but with larger range (see Fig. 7). The latter scanning method also allowed better examination of the tails of the focus in the cases where the source image grew too large for the range of the piezo table.

For imaging the 106-K-nozzle beam source we used a silicon-nitride zone plate (ZP_1), which was fabricated at MIT's NanoStructures laboratory [32] using electron-beam lithography and is shown in Fig. 3. The diffraction grating must be free-standing to allow the passage of the low-energy molecules. The grating bars are held in place by a radial support structure. The focal length of zone plate ZP_1 is $f = 477.3$ mm at a de Broglie wavelength of 97.8 pm. It has a diameter of 388 μm. The inner zones up to a radius of 70 μm are blocked to remove the zeroth diffraction order close to the beam axis, where the first-order focus is located. Since the zeroth diffraction order contains 25% of the intensity incident on the zone plate and the first diffraction order only about 10%, blocking the former increases the signal-to-noise ratio for the focus scan. This is especially important in imaging experiments [16]. The zone plate has a thickness of about 150 nm. In the focusing experiments using this zone plate we used a source-to-zone-plate distance of $g = (1550 \pm 10)$ mm and the distance from the zone plate to the aperture on the piezo table was $b = (809 \pm 10)$ mm.

For focusing the 310-K-nozzle beam we used a free-standing nickel zone plate (ZP_2). It is the same as ZP_2 in our previous article on the helium virtual source [25]. ZP_2 was fabricated at the Institute for x-ray Physics at the University of Göttingen. It has a diameter of 540 μm and a focal length of $f = 506$ mm at a de Broglie wavelength of 53 pm. For this zone plate the inner 240 zones (up to a radius of 81 μm) are blocked to remove the zeroth diffraction order. The fabrication process is described by Rehbein [33]. The source distance $g = (1550 \pm 10)$ mm was the same as in the cold-nozzle experiments, while the image distance was slightly longer at $b = 836 \pm 10$ mm. Previous experiments with this zone plate have shown that zones outside of a diameter of about 430 μm are not transparent [16].

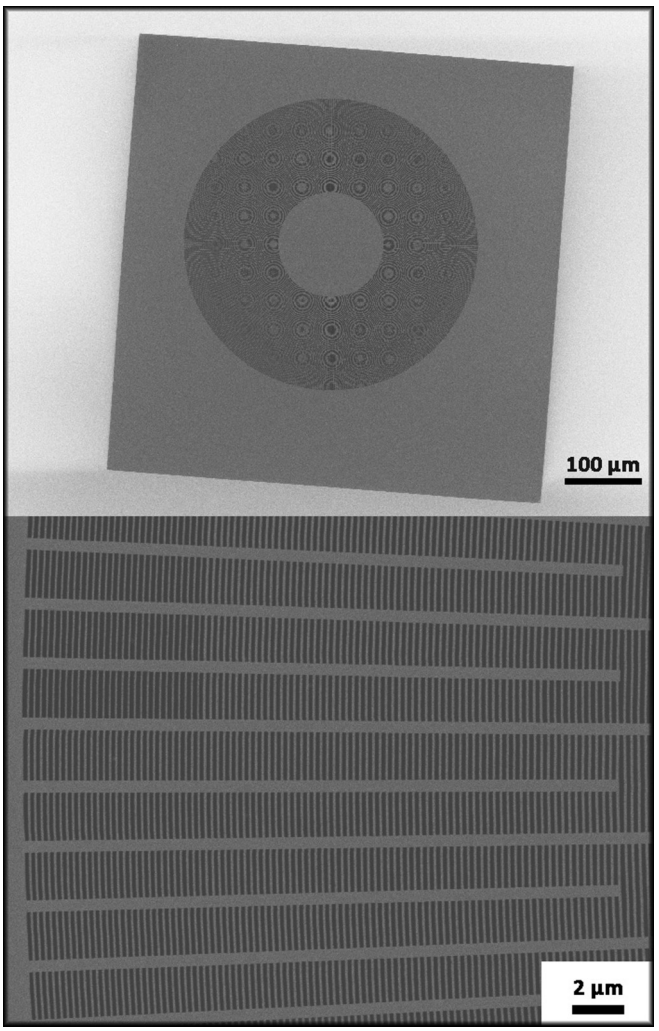

FIG. 3. Scanning-electron micrographs of the free-standing silicon-nitride zone plate used for imaging the cold-nozzle source. In the top image one can see the entire zone plate with a diameter of 388 μm. The central disk with a diameter of 140-μm blocks the zeroth diffraction order close to the optical axis. The grating pattern is not resolved, but instead circular Moiré fringes are visible. The edges of the square-shaped silicon-nitride membrane (600 μm width and about 150 nm thickness) into which the zone plate pattern was etched, shows significantly darker than the surrounding part of the silicon substrate. In the lower image the outer grating bars (approximately vertical) of the zone plate are magnified. The outermost transparent zone has a width of 120 nm. The horizontal bars with a width of about 450 nm are the support bars upholding the free-standing grating structure.

The most probable de Broglie wavelength was in the range of 86.8 ± 0.1 pm to 90.5 ± 0.1 pm for the cold-nozzle beam and 47.9 ± 0.1 pm to 53.1 ± 0.1 pm for the warm-nozzle beam. The speed ratio ranged from 10.5 ± 0.2 to 33.5 ± 0.2 (warm nozzle) and from 17.0 ± 0.1 to 25.4 ± 0.1 (cold nozzle)

with the peak at $p_0 = 20$ bars due to condensation, as is explained in the following sections. The relatively broad speed distribution makes it difficult to measure the exact position of the optimal focal plane. For this reason it was decided to keep the imaging distance b constant despite of the changing wavelength. To compensate for this we developed an accurate model of the zone plate focus and used that to deconvolve the measured focus widths. The effect of van der Waals forces on the focusing properties of the zone plates is only a change in the ratio between the widths of open and blocked Fresnel zones, which is very small due to the small polarizability of D_2 and the short interaction distance (thickness of the zone plates) [32].

III. THEORETICAL MODEL FOR DEUTERIUM EXPANSION

A theoretical description of the expansion is developed for predicting the behavior of deuterium beams such as terminal speed, speed ratio, and virtual source size. The model was inspired by the work of Winkelmann [34] on hydrogen in which a decoupling between translational and rotational relaxation was assumed and its expansion was treated with the same method employed for a monoatomic gas [25]. We apply Winkelmann's model to D_2 using its specific quantum mechanical properties as well as its real-gas properties. Additionally, we include the coupling between translation and rotation explicitly [35].

The evolution during the expansion of the velocity distribution $f(\vec{v})$ can be calculated by solving the Boltzmann equation by using an approximated method [36,37]. The expansion is assumed to be spherically symmetric and therefore flow properties depend only on the distance from the source. Furthermore, an anisotropic velocity distribution is assumed, which is the product of two Maxwellian functions with two temperatures, $T_{||}$ and $T_\perp$, respectively, to describe the different behavior of velocity components parallel ($v_{||}$) and perpendicular ($v_\perp$) to the streamlines,

$$f(\vec{v}) = n\left(\frac{m}{2\pi k_b T_{||}}\right)^{\frac{1}{2}}\left(\frac{m}{2\pi k_b T_\perp}\right) \times \exp\left(-\frac{m}{2k_b T_{||}}(v_{||}-u)^2 - \frac{m}{2k_b T_\perp}v_\perp^2\right), \quad (1)$$

where m is the deuterium mass, k_b is the Boltzmann constant, n is the molecular density, and u is the most probable velocity of the gas.

Inserting this expression for the velocity distribution in the Boltzmann equation it is possible to calculate an approximate solution for the gas and obtain parameters such as the speed ratio $S = \sqrt{\frac{1}{2}mu^2/k_b T_{||}}$, which describes the width of the parallel velocity distribution. The translational-rotational coupling is evaluated following the model introduced by Klots [35], in which a rotational temperature T_R is used to describe the rotational energy of the deuterium molecules and the relaxation relationship is given by

$$\frac{dT_R}{dt} = -\frac{T_R - \bar{T}}{\tau}, \quad (2)$$

where $\bar{T} = (2T_\perp + T_{||})/3$ is the mean kinetic temperature and τ the relaxation time.

The evolution of the parameters $n, u, T_R, T_{||}$, and $T_\perp$ is obtained by solving numerically with the method of moments [38] the set of four coupled integro-differential equations, derived from the Boltzmann equation for the monoatomic gas modified by the translational-rotational coupling terms and including the rotational energy E_R in the conservation of energy, and the fifth equation for the derivative of T_R:

$$\frac{d}{dr}(nur^2) = 0, \quad (3)$$

$$\frac{d}{dr}\left[u^2 + \left(\frac{3k_b T_{||}}{m}\right) + \left(\frac{2k_b T_\perp}{m}\right) + \frac{E_R}{m}\right] = 0, \quad (4)$$

$$\frac{dT_{||}}{dr} = -\frac{mu}{k_b}\frac{du}{dr} - \frac{T_{||}}{n}\frac{dn}{dr} - \frac{2}{r}(T_{||} - T_\perp) + \frac{2}{3u\tau}(T_R - \bar{T})\left[1 + \left(\frac{T_{||} - T_\perp}{9\,\bar{T}}\right)\right], \quad (5)$$

$$\frac{dT_\perp}{dr} = \frac{m\langle \Delta v_\perp^2\rangle}{2nuk_b} - \frac{2}{r}T_\perp + \frac{2}{3u\tau}(T_R - \bar{T})\left[1 - \left(\frac{T_{||} - T_\perp}{18\bar{T}}\right)\right], \quad (6)$$

$$\frac{dT_R}{dr} = -\frac{T_R - \bar{T}}{u\tau}, \quad (7)$$

where r is the reduced distance from the source $r = \frac{x}{d_{nz}}$, and x is the distance from the source. The term $\langle \Delta v_\perp^2\rangle$ contains the collision integral

$$\Omega^{(2,1)}(T) = \left(\frac{k_b T}{\pi m}\right)^{(1/2)}\int_0^\infty Q^{(2)}(E)\gamma_E^5 \exp\left(-\gamma_E^2\right)d\gamma_E, \quad (8)$$

$$\gamma_E = \sqrt{\frac{E}{k_b T}}, \quad (9)$$

where $Q^{(2)}$ is the viscosity cross section and E is the collision energy of two atoms in the center-of-mass system.

We have calculated the scattering cross section and the associated collision integral taking into account quantum effects. For collisions between Bose-Einstein particles,

$$Q^{(2)}(E) = \frac{8\pi\hbar^2}{mE}\sum_{l=0,2,4,\ldots}\frac{(l+1)(l+2)}{(2l+3)}\sin^2(\eta_{l+2} - \eta_l), \quad (10)$$

where η_l is the phase shift of the partial wave with orbital angular momentum l. Phase shifts are estimated employing the computation procedure described in detail in Ref. [39] and the Numerov method [40,41] is used for the numerical integration of the Schrödinger equation. In order to describe the deuterium interaction, two potential curves have been considered which are the isotropic part of the full interaction potential. The well-known Lennard-Jones (12-6) potential (we refer to it as LJ potential) is expressed as

$$V^{\mathrm{LJ}}(R) = 4\epsilon\left[\left(\frac{\sigma_0}{R}\right)^{12} - \left(\frac{\sigma_0}{R}\right)^{6}\right], \quad (11)$$

where R is the interatomic distance, $\epsilon = 3.1626$ meV is the well depth, and $\sigma_0 = 2.959$ Å is the position where

the potential vanishes and for shorter distances becomes positive [27].

The other potential by Buck *et al.* [28] is expressed as the sum of repulsive and attractive contributions and is referred to as the BK potential from here onwards:

$$V^{\mathrm{BK}}(R) = A\exp[-\beta R - \eta R^2] - (C_6/R^6 + C_8/R^8 + C_{10}/R^{10})D(R), \quad (12)$$

with

$$D(R) = \begin{cases} \exp[-(G/R-1)^2], & R \leqslant G; \\ 1, & R > G. \end{cases} \quad (13)$$

The parameters are

$$A = 101.4\ \mathrm{eV},\quad \beta = 2.779\ \text{Å}^{-1},\quad \eta = 0.08\ \text{Å}^{-2},$$
$$G = 5.102\ \text{Å},\quad C_6 = 7.254\ \mathrm{eV\,Å}^6,\quad C_8 = 36.008\ \mathrm{eV\,Å}^8,$$
$$C_{10} = 225.56\ \mathrm{eV\,Å}^{10}. \quad (14)$$

The solution of the coupled integro-differential equations can be calculated by means of the standard Runge-Kutta computation procedure [42]. During the expansion, energy transfer between rotational and translational degrees of freedom generally requires several collisions, the relaxation time therefore can be expressed as $\tau^{-1} = 2.4n\xi\Omega^{(2,1)}(T_R)$ [43], where the scaling coefficient ξ is the inverse of the number of collisions which are necessary for the transfer. In the calculations ξ can be treated as a free parameter but we have used the values estimated in Ref. [44], that is, $\xi^{-1} = 576$ and 150 at $T = 101$ K and 310 K, respectively.

The integration of the integro-differential equations is started at $r = 0.591$ value suggested as the boundary condition for the thermal conduction model of Klots [43]. The starting parameters are obtained from the source conditions, T_0 and p_0, using the analytical formula of Ref. [45] for the isentropic expanding gas with $\gamma = C_P/C_V = 1.4$ and the real thermodynamic properties of deuterium provided by Prydz *et al.* [46]. At this point all the temperatures are assumed equal, that is, $T_R = T_\perp = T_{||}$, which seems to be a good approximation since the gas density and in turn the collision frequency are still high enough to assure a local equilibrium. The distance at which the integration is terminated (distance of the quitting surface from the nozzle, D_{qs}, where the collision frequency is negligible) is somewhat arbitrary. In the present calculation we use the criterion $T_\perp/T_{||} < 0.01$ to stop the calculations as in the case of He [47].

At the end of the expansion, the physical parameters are estimated from the beam temperatures. For the virtual source width w_s we have [25]

$$w_s = 2\sqrt{2\ln 2}\ \frac{D_{\mathrm{qs}}}{u}\sqrt{k_B T_\perp/m}. \quad (15)$$

The beam temperatures calculated using the model are shown as a function of source pressure in Fig. 4 for the BK potential and a source temperature of $T_0^c = 301.4$ K. Since the temperature sensor attached to the nozzle does not directly measure the gas temperature, we used a temperature different from the measured one, determined by the terminal speed, for the calculations. We refer to the temperature measured by the sensor with T_0 and to the temperature assumed in the model with T_0^c. Just as in the case of the helium expansion [25] the perpendicular temperature calculated using the solution of the integro-differential equations does not describe the virtual source width very well (see section on virtual source width). However, terminal speed and speed ratio are very well described by the model (see sections on speed and speed ratio). For this reason we have only attempted to estimate the perpendicular temperature of the beam at the quitting surface, separately, using continuum scaling laws. Since D_2 is biatomic but the calculations were performed for a monoatomic gas, we have considered both the mono- and biatomic cases. For an axisymmetric expansion in the continuum region with the reduced distance from the source $r > 4$, the perpendicular temperature $T_\perp$ depends on the distance as [1]

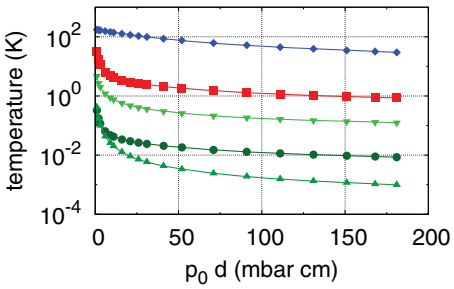

FIG. 4. (Color online) Temperatures of a D_2 beam with nozzle at $T_0^c = 301.4$ K calculated using the BK potential at the end of the expansion. The blue (♦) line corresponds to the rotational temperature of the molecular beam. The red (■) line corresponds to the parallel temperature. The dark-green (●) line gives the perpendicular temperature calculated using solution of the integro-differential equations. For the medium-green (▲) line the perpendicular temperature was calculated using monoatomic continuum scaling laws and for the light-green (▼) line it was biatomic continuum scaling laws.

$$T_\perp^{\mathrm{mono}}(r) = 0.287 \times T_0 r^{-\frac{4}{3}} \quad (16)$$

for a monoatomic gas and

$$T_\perp^{\mathrm{bi}}(r) = 0.385 \times T_0 r^{-\frac{4}{5}} \quad (17)$$

for a biatomic gas. These continuum perpendicular temperatures are also shown in Fig. 4 and the resulting virtual source widths were compared to the experimental data in one of the next sections.

IV. TERMINAL SPEED

In Fig. 5(a) we present the theoretical model prediction for the terminal speed of the 310-K-nozzle deuterium beam together with the experimental data from the TOF experiments. We expect a certain deviation of the measured nozzle temperature T_0 from the actual initial temperature of the expansion T_0^c that is used for the model, as mentioned previously. The measurement of the terminal speed can be taken as a very good indicator for the actual temperature of the expansion. Similarly, in the recent study by Ekinci *et al.* [48] the nozzle temperatures had to be corrected downwards by 13 K for their three colder nozzle conditions. We have evaluated the expansion model over a range of temperatures at a resolution of 0.1 K and thus found T_0^c for each interaction potential with the least-squares

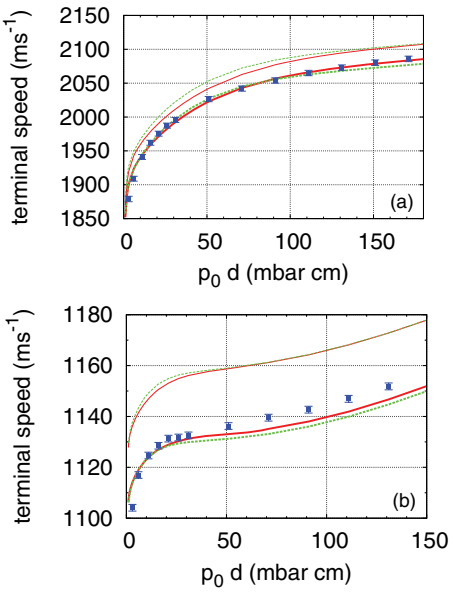

FIG. 5. (Color online) Terminal speed of D_2 beam with nozzle at $T_0 = 310$ K (a) and at $T_0 = 106$ K (b). The squares (■) show the results of the TOF measurements. The model calculation at $T_0^c = 303.6$ K (a) and $T_0^c = 102.2$ K (b) using the LJ potential is displayed as the continuous (red) line. The result corresponding to the BK potential with $T_0^c = 301.4$ K (a) and $T_0^c = 101.9$ K (b) is given as the dashed (green) line. The corresponding thin lines show the model result for the measured nozzle temperature $T_0 = 310$ K (a) and $T_0 = 106$ K (b). Note that the increase in terminal speed at pressures above about $p_0 = 40$ bars in (b) is mainly due to the real-gas properties of D_2.

deviation from the measured terminal speed values. The result of this optimization is shown in Table I. The data points below a pressure of 3 bars were excluded from this optimization, due to the large relative uncertainty in setting the beam pressure of about 50%.

The terminal speed data for the 106-K-nozzle beam in the current study are presented in Fig. 5(b). At the same cold source conditions we have recorded mass spectra (see reference [30]) which showed signs of cluster condensation already at $p_0 = 3$ bars. The additional heat released from cluster condensation results in an increased terminal speed. Since the expansion model does not take into account condensation, we do not expect the model to accurately predict terminal speed in presence of condensation. The optimized temperature values in Table I were therefore obtained by restricting the data set to pressures $p_0 = 6$, 11, and 16 bars. It is satisfying to see that the measured terminal speed increases faster than the model also at these low pressures, consistent with the observation of clusters in the mass spectra.

TABLE I. Optimized nozzle temperatures based on a least-squares fit of the expansion-model terminal speeds to the experimental data.

T_0 (K)	Potential	T_0^c (K)
310	LJ	303.6
310	BK	301.4
106	LJ	102.2
106	BK	101.9

V. TERMINAL SPEED RATIO

The terminal random-translational enthalpy parallel to the beam axis of the beam is characterized using its speed ratio S (see section on the theoretical model). From the TOF spectrum S is derived using the equation,

$$S = 2\sqrt{2\ln 2}\frac{u}{\Delta u} \approx 2\sqrt{2\ln 2}\frac{t}{\Delta t}, \tag{18}$$

where Δu and Δt refer to the FWHM of the terminal speed and TOF distributions, respectively. The result of the theoretical model using the nozzle temperature and experimental data from the TOF experiments for the warm-nozzle beam are shown in Fig. 6(a). The model predicts the trend of the measured speed ratios very well, but underestimates it by 5%–20% (excluding the data point at the lowest source pressure). This deviation could be caused by a systematic error in the calibration of the FWHM of the TOF data. The BK potential gives a better correspondence to the experimental data.

In Fig. 6(b) we present the terminal speed-ratio results for the cold-nozzle beam. The experimental data peaks at around 21 bars nozzle pressure, and then stabilizes at a speed-ratio of about 22 at a stagnation pressure of about 40 bars, as previously observed [48]. The reduction in the speed ratio is due to an increase in the random-translational enthalpy caused by the cluster condensation. For the three data points at the nozzle pressures that we also used for the optimization of T_0^c the model prediction fits almost perfectly for the LJ potential. However, these three points are to some extent affected by condensation. Observing that condensation reduces the speed ratio for points at higher pressure we may presume that also these points should be higher without condensation. Therefore, the good agreement with the LJ potential is likely fortuitous and the agreement with the BK potential may be better. In this case it is not possible to decide which potential provides the better agreement.

VI. POINT-SPREAD FUNCTION OF THE ZONE PLATES

The measured spot profile of Fig. 7 presents tails that cannot be fitted by a single Gaussian function. To retrieve the FWHM of the virtual source from the focusing data we used nonlinear least-square fitting of a zone-plate diffraction model. For this we assumed that the image of the virtual source is described by the sum of two Gaussian functions $G_1(x,y)$ and $G_2(x,y)$ with FWHM w_1 and w_2 and equal normalization factor A. Choosing the normalization factor of both Gaussians as free parameters, as can be found in the literature [24], results in large correlation between the two parameters.

The diffraction model uses the measured and corrected (see above) TOF distribution to calculate the corresponding de Broglie wavelength distribution for each nozzle temperature and pressure. This distribution is then sampled uniformly at a resolution of 0.1 pm. For each specific wavelength we have calculated the point-source diffraction pattern in the imaging plane of the experiment, using an adaptation of

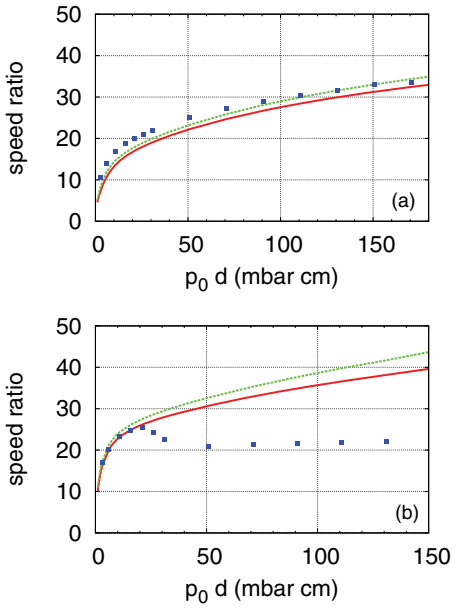

FIG. 6. (Color online) Terminal speed ratio of D_2 beam with nozzle at $T_0 = 310$ K (a) and at $T_0 = 106$ K (b). The squares (■) show the results of the TOF measurements. The uncertainty of the terminal speed ratio is ±0.2 in (a) and ±0.1 in (b). The model calculation at $T_0^c = 303.6$ K (a) and $T_0^c = 102.2$ K (b) using the LJ potential is displayed as the continuous (red) line and the result corresponding to the BK potential at $T_0^c = 301.4$ K (a) and $T_0^c = 101.9$ K (b) is given as the dashed (green) line. At a pressure of about 21 bars for the low-temperature nozzle (b) condensation effects become significant, resulting in an obvious reduction of speed ratio.

Dauger's algorithm for calculating Fresnel diffraction patterns (see Fig. 8) [49]. The implementation takes into account the central blocking disk but not the support bars. However, the support bars block only about 12% of the zone plate's area. Also, the support bars have radial symmetry so that their effect on the focus is mainly an attenuation by those 12%. The sum of the diffraction patterns, weighted in accordance with the wavelength distribution, results in a two-dimensional diffraction image that corresponds to the PSF $F_{PS}(x,y)$ of the zone plate. The PSF is then convoluted with a two-dimensional aperture function $H(x,y)$ corresponding to the 10-μm-diameter detector aperture and finally we consider the section through the maximum of the convoluted PSF. An example of the resulting distribution is shown in Fig. 7 as the dash-dotted (black) line. Finally the following function is fitted to the focus data,

$$I_0 + [G_1(x,0) + G_2(x,0)] * (F_{PS} * H)(x,0), \qquad (19)$$

where the detector background I_0 was determined in a separate measurement and $*$ denotes convolution. The free parameters were w_1, w_2, and A. To be able to compare the result with the expansion model described in the theory section, we used the standard deviation in x of the intensity function $G_1(x,0) + G_2(x,0)$, and multiplied it by the factor $2\sqrt{2\ln 2}$ to give the FWHM of a single Gaussian of equal standard deviation. This single-Gaussian-equivalent FWHM is then divided by the magnification $M = b/g$ to give the measured virtual source width.

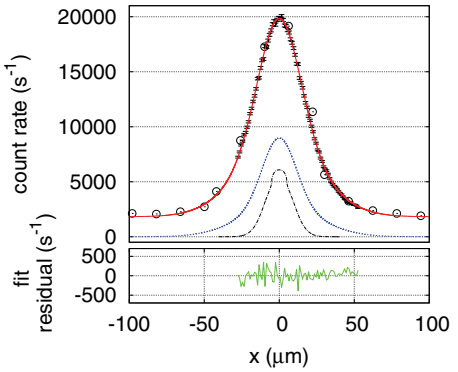

FIG. 7. (Color online) In the top graph the zone-plate focus of the deuterium beam with source conditions $p_0 = 150$ bars and $T_0 = 310$ K is shown. Experimental data (⊙) were collected by stepping the circular aperture horizontally across the center of the experimental image (maximum of the intensity) using detector arm rotation. The uncertainty in x for this data set is about 5 μm. Scanning the same region using the piezo table while keeping the detector arm stationary resulted in the data set shown with black error bars. For both data sets a vertical (orthogonal) scan with the piezo table was recorded to locate the vertical center of the experimental image. The uncertainty in x for the piezo-table data set is about 0.02 μm. The continuous (red) line shows the result of the least-squares fit of Eq. (19) to the piezo-table data. The dashed (blue) line shows the deconvolved focus $G_1 + G_2$ based on the parameters resulting from the fit described in the text. The dash-dotted (black) line gives the diffraction-model result $F_{PS} * H$. The continuous (green) line in the bottom graph shows the fit residuals.

VII. VIRTUAL-SOURCE SIZE

The virtual source size of the molecular beam is a function of the perpendicular beam temperature or the random translational enthalpy perpendicular to the beam-axis at the quitting surface. As mentioned in the expansion-model section we used three different methods to calculate the perpendicular

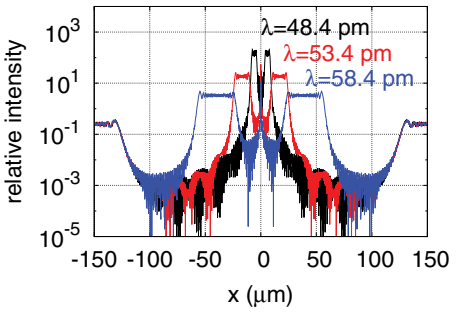

FIG. 8. (Color online) In this figure we show the calculated lateral intensity of the point-source diffraction pattern in the imaging plane for three different wavelengths and relative to the undisturbed beam intensity. Note the logarithmic scale on the y axis. The zeroth diffraction order which can be seen at a distance greater than about 120 μm from the central axis and has the expected relative intensity of 0.25 on average. The first-order focus includes a shadow due to the central stopping disk of the zone plate. On the central axis one can notice a Poisson spot. For the focus model we calculated a diffraction pattern of this type every 0.1 pm in the wavelength ranges 43.4–65.6 pm (warm nozzle) and 82.8–106.8 pm (cold nozzle).

beam temperature. It is not surprising that the solution of the Boltzmann equation gives a poor estimate for $T_\perp$ at the quitting surface, and thus a poor estimate for the virtual-source size. As collisions decrease during the expansion the different degrees of freedom are increasingly decoupled and particularly the perpendicular degrees of freedom exhibit nonequilibrium behavior [23]. This means that the perpendicular speed distribution is no longer described by a simple Gauss distribution. As a result, the virtual source cannot be described as a single Gauss function either, as is reflected by the fit of the experimental virtual source data.

The theoretical and experimental results for the virtual source width of the warm-nozzle beam are given in Fig. 9(a). The deconvolved widths of both the narrow and broad virtual-source components [$G_1(x,y)$ and $G_2(x,y)$] are shown. For our data the single-Gauss-equivalent FWHM (see previous section), which is shown as large (blue) squares in Fig. 9(a), tends to be slightly larger than the average of the narrow and broad component's FWHM. With this interpretation the experimental data fit very well with the assumption of a monoatomic continuum-expansion scaling of the perpendicular temperature calculated at a quitting-surface distance given by the solution of the Boltzmann equation.

At the two lowest pressures especially the broader source increases in width. We do not believe that this is a physical effect but rather caused by the stronger dependence of the terminal speed on nozzle pressure and the large relative uncertainty of the nozzle pressure reading. In fact, TOF data and the focusing data were recorded in different runs and slightly different source pressures might result in an unaccounted-for increase in image size of the virtual source due to chromatic aberration.

The results for the cold-nozzle beam are shown in Fig. 9(b). As in the warm-nozzle case the perpendicular temperature is best described by a monoatomic continuum-expansion scaling terminated at the quitting surface. Similar to the terminal speed and speed-ratio measurement we note an increasing deviation between model and experiment above about $p_0 = 21$ bars due to cluster condensation. Below this condensation threshold the model predicts a virtual source size which is almost twice the experimental single-Gaussian equivalent value. Although the agreement is reasonable for the purpose of the estimation of beam parameters and at most limits the model applicability to temperatures above 110 K, this discrepancy points at an increased cooling of the perpendicular degrees of freedom at the low-temperature source conditions. This could be explained by an overestimate of the distance of the expansion-model quitting surface from the nozzle. However, with monoatomic cooling the width of the source is proportional to $r^{1/3}$ (with $r = D_{qs}$) and thus the quitting surface would have to be moved closer to the nozzle by a factor of 8 to explain the deviation. This is not likely as it would cause a large change in the predictions of speed and speed ratio which are predicted very well by the model. Another possible explanation could be that the perpendicular velocity distribution would require a better description of the long tails (kurtosis) directly in the calculations replacing the Gaussian with a suitable distribution: This will increase the complexity of the model and will be tried in future investigations.

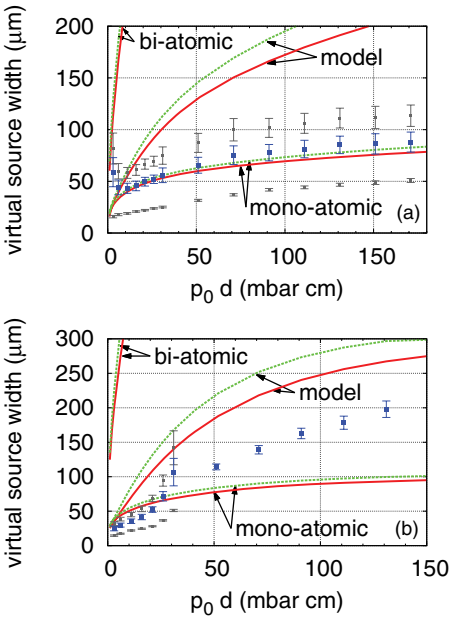

FIG. 9. (Color online) Virtual source width of D_2 beam with nozzle at $T_0 = 310$ K (a) and $T_0 = 106$ K (b). The image of the virtual source was created using a free-standing Fresnel zone plate at a magnification of 0.54 (a) and 0.52 (b). The small (gray) squares (■) with error bars show the result of the deconvolved narrow and broad virtual-source widths. The large (blue) squares (■) with error bars show the single-Gaussian-equivalent FWHM (see text). The uncertainty of the virtual source widths is derived from the least-squares fit. The model calculations at $T_0^c = 303.6$ K (a) and $T_0^c = 102.2$ K (b) using the LJ potential are displayed as continuous (red) lines and the results corresponding to the BK potential at $T_0^c = 301.4$ K (a) and $T_0^c = 101.9$ K (b) are given as dashed (green) lines. The labels indicate the method used to derive the perpendicular temperature at the quitting surface (see text). In (b) condensation effects additionally contribute to the increase of virtual source size starting at a source pressure of about 20 bars. In the same graph at source pressures of $p_0 = 51$ bars and above the least-square fitting procedure of the focus data would no longer converge despite including the less accurate but wider range detector-arm scan points in the fit. For this reason the source-model was reduced to a single Gaussian $G_1(x,0)$ for those points.

VIII. D_2 INTERACTION POTENTIAL

With the careful uncertainty analysis we have performed it is possible to evaluate the performance of the two different interaction potentials in predicting terminal speed, speed ratio, and virtual-source size. In the case of the warm-nozzle beam the contributions from any clustering are negligible and therefore we expect perfect correspondence with the experimental data. In Table II we have calculated the reduced χ^2 based on the residuals between experimental data and the corresponding theoretical values. The lowest source-pressure data point were again neglected, due to its comparatively larger relative uncertainty.

From the table we see that the speed data, for which the model was fitted via the nozzle temperature, are almost equally well reproduced by the two potentials. However, the speed-ratio and virtual-source data are clearly better reproduced by the BK potential (smaller χ^2 values). The χ^2 values for the

TABLE II. Reduced χ^2 values for experimental data with respect to model prediction for the two different D_2 interaction potentials. u refers to terminal speed, S to terminal speed- ratio, and w_s to the width of the virtual source.

Potential	$\chi^2(u)$	$\chi^2(S)$	$\chi^2(w_s)$
LJ	2.1	334	1.0
BK	2.6	131	0.4

speed-ratio data are relatively large, which could be due to an unaccounted for systematic error, considering that the trend of the data is reproduced rather well by the model. For the cold-nozzle data there are only three data points (at $p_0 = 6, 11$, and 16 bars) for which condensation has a limited influence. The χ^2 values of the speed-ratio data favor the LJ potential but this may change in the presence of condensation toward the BK potential. Overall, we note a preference for the BK potential.

IX. VIRTUAL-SOURCE BRIGHTNESS

The brightness of beam sources is an important parameter in many applications. In Fig. 10 we therefore report the brightness of the D_2 virtual source as determined from the zone-plate focusing experiments. The brightness B as a function of the total intensity in the focus I_f and the area of the virtual source A_{vs} is given by

$$B = \frac{I_f}{A_{vs}} \frac{1}{\Omega_{zp}} \frac{1}{\eta_{zp}} \frac{1}{\eta_{det}}, \tag{20}$$

where Ω_{zp} is the solid angle under which the source illuminates the zone plate. η_{det} and η_{zp} are the efficiencies of the detector and the zone plate, respectively. The latter was determined in separate experiments and takes into account both the support structure and the central block. For the Göttingen zone plate (warm-nozzle beam) the efficiency is $\eta_{zp} = 0.033 \pm 0.007$ and for the MIT zone plate it is $\eta_{zp} = 0.047 \pm 0.005$. The efficiency of the detector for D_2 was estimated to be $\eta_{det} = (5 \pm 1) \times 10^{-6}$ [31].

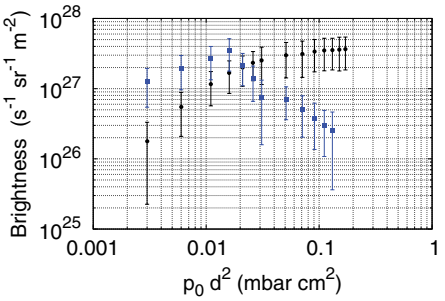

FIG. 10. (Color online) The graph displays the brightness of a D_2 supersonic expansion for source temperature $T_0 = 310$ K with solid (black) bullets (•) and for source temperature $T_0 = 106$ K with large (blue) squares (■). The uncertainty indicated by the error bars is determined from the uncertainties in the quantities used to determine the values (see text). For both source temperatures approximately the same brightness is reached. For the cold-nozzle conditions clustering is to be blamed for the sharp decrease in brightness at higher source pressures.

The brightness of the helium virtual source reported in Ref. [25] was likely an overestimate due to the then poorly known transmission characteristics of the zone plate. The reported brightness for the helium jet would then also better correspond to the values reported by De Ponte *et al.* [24] of about 10^{27} s^{-1} sr^{-1} m^{-2} for a 9.5-μm-diameter nozzle. This suggests that the D_2 virtual source is at least a factor 2 brighter than the helium source under similar conditions.

X. CONCLUSION

We have investigated the supersonic expansion of D_2 at two distinct source temperatures ($T_0 = 106$ K and $T_0 = 310$ K) and over a wide range of source pressures and also developed a model to predict properties of the resulting beam. Terminal speed and speed ratio were obtained by TOF experiments while virtual source sizes were estimated by a careful least-squares fitting deconvolution procedure using the setups PSF specific to each source condition and zone-plate focusing experiment.

Varying the source temperature used in the expansion model resulted in excellent agreement with the terminal speed data at all source conditions where cluster condensation was negligible. The correspondence with terminal speed-ratio data was good as well, although we observed a small systematic deviation. The virtual-source-width data were reproduced very well for the warm-nozzle beam, when taking into account the model's inability to duplicate the nonequilibrium behavior of the degrees of freedom perpendicular to the beam axis and instead calculating the perpendicular beam temperature using a monoatomic scaling law. The biatomic scaling law did not reproduce virtual source size data well, which indicates that the rotational degrees of freedom do not play a role in the cooling of the perpendicular temperature. This is very probably because the deuterium rotational levels are well spaced and in the low temperature of the expanding beam the rotational excitations are limited to very few levels so that the gas behaves essentially as a monoatomic one. For the cold-nozzle beam the virtual source is by almost a factor two narrower than the model's monoatomic-scaling prediction (for the region were condensation effects are small). Virtual source widths ranged from 14.7 ± 0.5 μm to 190.2 ± 0.5 μm for the cold-nozzle beam and from 23.4 ± 0.5 μm to 70.1 ± 0.5 μm for the warm-nozzle beam.

After careful analysis of the experimental data we find that the interaction potential by Buck *et al.* [28] is moderately better at predicting the properties of the D_2 supersonic expansion. To draw a clearer conclusion it will be necessary to include condensation effects in the theoretical model. Such a model, when compared to experimental data, could then also provide insight into condensation energies of various cluster sizes. Furthermore, it would be interesting to study the expansion's properties at even higher flow rates where the interaction potentials result in larger deviating predictions with respect to each other.

Finally, we report the brightness of the D_2 supersonic expansion for the studied source conditions. The maximum brightness is for both source temperatures at about $(3 \pm 1) \times 10^{27}$ s^{-1} sr^{-1} m^{-2} which is about a factor 2 to 3 brighter than the brightness of a helium supersonic-expansion source at similar source conditions. In the future we plan to study

the brightness of sources with smaller nozzle diameter and at higher stagnation pressures with the hope of further improving the brightness of supersonic-expansion sources.

ACKNOWLEDGMENTS

This project was funded by the Bergen Research Foundation. One of the authors (G.B.) was supported by the Christian Michelsen Center for industrial measurement science and technology (MIMT) in Bergen. The Fresnel zone plate that was used to focus the 310 K nozzle beam was fabricated at the Institute for X-ray Physics, University of Göttingen, by Stefan Rehbein and Günter Schmahl. The other zone plate was fabricated by one of the authors (T.R.) at the NanoStructures Laboratory, Massachusetts Institute of Technology, under the supervision of Henry I. Smith. The molecular-beam apparatus was designed and assembled at the Max-Planck Institute (MPI) for fluid dynamics (now called MPI for dynamics and self-assembly) in Göttingen and is now located at the University of Bergen.

[1] H. Pauly, *Atom, Molecule and Cluster Beams I*, Vol. 1 (Springer, Berlin, 2002).
[2] D. Farias and K.-H. Rieder, Rep. Prog. Phys. **61**, 1575 (1998).
[3] Edited by G. Scoles, *Atomic and Molecular Beam Methods* (Oxford University Press, Oxford, 1998).
[4] Edited by R. Campargue, *Atomic and Molecular Beams* (Springer, Berlin, 2001).
[5] F. Hofmann and J. P. Toennies, Chem. Rev. **96**, 1307 (1996).
[6] G. Bracco, J. Acker, M. D. Ward, and G. Scoles, Langmuir **18**, 5551 (2002).
[7] L. Pedemonte, G. Bracco, C. Boragno, F. B. de Mongeot, and U. Valbusa, Phys. Rev. B **68**, 115431 (2003).
[8] J. Frenken, B. Hinch, and J. Toennies, Surf. Sci. **211-212**, 21 (1989).
[9] F. Traeger, ChemPhysChem **7**, 1006 (2006).
[10] W. Steurer, A. Apfolter, M. Koch, W. E. Ernst, B. Holst, E. Søndergård, and J. R. Manson, Phys. Rev. Lett. **99**, 035503 (2007).
[11] W. Steurer, A. Apfolter, M. Koch, T. Sarlat, E. Søndergård, W. Ernst, and B. Holst, Surf. Sci. **601**, 4407 (2007).
[12] R. B. Doak, R. E. Grisenti, S. Rehbein, G. Schmahl, J. P. Toennies, and C. Wöll, Phys. Rev. Lett. **83**, 4229 (1999).
[13] B. Holst and W. Allison, Nature (London) **390**, 244 (1997).
[14] K. Fladischer, H. Reingruber, T. Reisinger, V. Mayrhofer, W. E. Ernst, A. E. Ross, D. A. MacLaren, W. Allison, D. Litwin, J. Galas *et al.*, New J. Phys. **12**, 033018 (2010).
[15] D. Barredo, G. Laurent, F. Calleja, P. Nieto, J. Hinarejos, A. de Parga, D. Farías, and R. Miranda, Appl. Phys. Lett. **96**, 081901 (2010).
[16] M. Koch, S. Rehbein, G. Schmahl, T. Reisinger, G. Bracco, W. E. Ernst, and B. Holst, J. Microsc. **229**, 1 (2008).
[17] P. Witham and E. Sánchez, Rev. Sci. Instrum. **82**, 103705 (2011).
[18] V. Soukhanovskii, H. Kugel, R. Kaita, R. Majeski, and A. Roquemore, Rev. Sci. Instrum. **75**, 4320 (2004).
[19] A. Täschner, E. Köhler, H.-W. Ortjohann, and A. Khoukaz, Nucl. Instrum. Methods Phys. Res., Sect. A **660**, 22 (2011).
[20] S. Dymov, V. Komarov, G. Macharashvili, Y. Uzikov, T. Azarian, O. Imambekov, A. Kulikov, V. Kurbatov, S. Merzliakov, B. Zalikhanov *et al.*, Phys. Rev. C **81**, 044001 (2010).
[21] T. Reisinger, A. A. Patel, H. Reingruber, K. Fladischer, W. E. Ernst, G. Bracco, H. I. Smith, and B. Holst, Phys. Rev. A **79**, 053823 (2009).
[22] R. E. Grisenti, W. Schöllkopf, J. P. Toennies, G. C. Hegerfeldt, and T. Köhler, Phys. Rev. Lett. **83**, 1755 (1999).
[23] H. Beijerinck and N. Verster, Physica B + C **111**, 327 (1981).
[24] D. P. DePonte, S. D. Kevan, and F. S. Patton, Rev. Sci. Inst. **77**, 055107 (2006).
[25] T. Reisinger, G. Bracco, S. Rehbein, G. Schmahl, W. E. Ernst, and B. Holst, J. Phys. Chem. A **111**, 12620 (2007).
[26] F. S. Patton, D. P. Deponte, G. S. Elliott, and S. D. Kevan, Phys. Rev. Lett. **97**, 013202 (2006).
[27] M. Zoppi, U. Bafile, E. Guarini, F. Barocchi, R. Magli, and M. Neumann, Phys. Rev. Lett. **75**, 1779 (1995).
[28] U. Buck, F. Kohlhase, and D. Otten, J. Chem. Phys. **78**, 4439 (1983).
[29] A. Apfolter, Master's thesis, Institute of Experimental Physics, Technical University, Graz, Austria, 2005.
[30] T. Reisinger, Ph.D. thesis, The University of Bergen, 2011.
[31] B. Samelin, Master's thesis, Georg-August-Universität zu Göttingen, MPI für Strömungsforschung, 1993.
[32] T. Reisinger, S. Eder, M. M. Greve, H. I. Smith, and B. Holst, Microelectron. Eng. **87**, 1011 (2010).
[33] S. Rehbein, J. Phys. IV **104**, 207 (2003).
[34] K. Winkelmann, *XI Symposium of Rarefied Gas Dynamics* (Commissariat A l'Energie Atomique, Paris, 1979), p. 899.
[35] C. E. Klots, Chem. Phys. **67**, 75 (1982).
[36] E. Knuth and S. Fisher, J. Chem. Phys. **48**, 1674 (1968).
[37] D. Miller and R. Andres, *VI Symposium of Rarefied Gas Dynamics*, Vol. 2 (Academic, New York, 1969), p. 1385.
[38] J. Toennies and K. Winkelmann, J. Chem. Phys. **66**, 3965 (1977).
[39] R. Bernstein, J. Chem. Phys. **33**, 795 (1960).
[40] B. Johnson, J. Chem. Phys. **67**, 4086 (1977).
[41] J. Gonzáleza and D. Thompsonb, Comput. Phys. **11**, 514 (1997).
[42] S. Mikhlin and K. Smolitsky, *Approximate Methods for Solution of Differential and Integral Equations* (American Elsevier, New York, 1967).
[43] L. K. Randeniya and M. A. Smith, J. Chem. Phys. **93**, 661 (1990).
[44] K. Kern, R. David, and G. Comsa, J. Chem. Phys. **82**, 5673 (1985).
[45] H. Murphy and D. Miller, J. Phys. Chem. **88**, 4474 (1984).
[46] R. Prydz, K. D. Timmerhaus, and R. B. Stewart, in *Proceedings of the 1967 Cryogenic Engineering Conference, Stanford University, Stanford CA*, edited by K. D. Timmerhaus (Plenum Press, New York, 1968), Vol. 13.
[47] L. Pedemonte and G. Bracco, J. Chem. Phys. **119**, 1433 (2003).
[48] Y. Ekinci, E. L. Knuth, and J. P. Toennies, J. Chem. Phys. **125**, 133409 (2006).
[49] D. E. Dauger, Comput. Phys. **10**, 591 (1996).